INSTITUT DE FRANCE
Académie des sciences

Comptes Rendus
Chimie

Mohamed Ali Mami, Marzouk Lajili and Tarek Echekki

CFD multiphase combustion modelling of oleic by-products pellets in a counter-current fixed bed combustor

Volume 25, Special Issue S2 (2022), p. 113-127

Published online: 29 March 2022

https://doi.org/10.5802/crchim.170

Part of Special Issue: Sustainable Biomass Resources for Environmental, Agronomic, Biomaterials and Energy Applications 3

Guest editors: Mejdi Jeguirim (Université de Haute-Alsace, Institut de Sciences des Matériaux de Mulhouse, France), Salah Jellali (Sultan Qaboos University, Oman) and Besma Khiari (Centre of Water Researches and Technologies, Tunisia)

This article is licensed under the
Creative Commons Attribution 4.0 International License.
http://creativecommons.org/licenses/by/4.0/

Les Comptes Rendus. Chimie *sont membres du*
Centre Mersenne pour l'édition scientifique ouverte
www.centre-mersenne.org
e-ISSN : 1878-1543

Comptes Rendus
Chimie
2022, Vol. 25, Special Issue S2, p. 113-127
https://doi.org/10.5802/crchim.170

Sustainable Biomass Resources for Environmental, Agronomic, Biomaterials and Energy Applications 3 / *Ressources de biomasse durables pour des applications environnementales, agronomiques, de biomatériaux et énergétiques 3*

CFD multiphase combustion modelling of oleic by-products pellets in a counter-current fixed bed combustor

Modélisation CFD de la combustion multiphases des pastilles de sous-produits oléiques dans une chambre de combustion à lit fixe à contre-courant

Mohamed Ali Mami [a], **Marzouk Lajili** [*, a] **and Tarek Echekki** [*, b]

[a] University of Monastir, Preparatory Institute of Engineering Studies of Monastir (IPEIM), Ionized and Reactive Media Studies Research Laboratory (EMIR), 15 Avenue Ibn El Jazzar Monastir 5019, Tunisia

[b] North Carolina State University, Department of Mechanical & Aerospace Engineering, 1840 Entrepreneur Drive Campus Box 7910 Raleigh, NC 27695-7910, USA

E-mails: hama.mami@yahoo.com (M. A. Mami), Marzouk.lajili@ipeim.rnu.tn, abouhechem@gmail.com (M. Lajili), techekk@ncsu.edu (T. Echekki)

Abstract. A transient two-dimensional multiphase model was built to study the combustion of pellets of oleic by-products (Olive Pits (OPi)) in a cylindrical counter-current 40 kW fixed bed combustor. The fixed bed is modelled as a porous medium, which is randomly packed with spherical particles of equal size. A $\kappa - \varepsilon$ model for low Reynolds number flows was used for turbulence Modelling. Primary and secondary air injections were supplied at the bed (solid phase combustion) and at the freeboard zone (gas phase combustion), respectively. The mass loss history, the temperature distribution at different heights inside the reactor and the gas emissions of CO, CO_2, O_2, H_2, CH_4 and C_{org} were computed. Key parameters related to the reaction front velocity, the mass conversion rate and the progress of ignition were also computed. We show that computational results are in good agreement with experimental measurements obtained using a similar reactor fed with the same pellet types. These results also motivate the implementation of the present formulation and its extension to industrial scale furnaces, having established the results for the comparison with pilot-scale experiments.

Keywords. CFD, Porous medium, Fixed bed reactor, Olive pits pellets, Multiphase combustion.
Published online: 29 March 2022

* Corresponding authors.

1. Introduction

Biomass when burned properly could be considered as a renewable and an environmentally friendly source of energy. Indeed, it can be used for the generation or the cogeneration of heat and/or electricity [1]. Biomass combustion is relatively complex to model due to the presence of reaction at different phases involving charcoal, tars and volatile mixtures of organic compounds. Moreover, the presence of large amounts of ash and minerals are a source of corrosion and slagging inside the combustion chamber. However, fixed bed reactors powered by solid fuels offer high automation and low costs. The Modelling and experimentation on the complex phenomena inside these reactors and the solid biomass conversion process must address the coupling of different processes, including heat and mass transfer, gas flow, moisture evaporation, pyrolysis and the combustion and the gasification processes. Yet, Computational Fluid Dynamics (CFD) of biomass combustion can provide important insight, and often complementary information to experiments, to these complex processes [2–4].

Details on the Modelling of biomass combustion as well as on the solid phase and on the gas phase reactions are reported in the literature [5–14]. Typically, a configuration consisting of two coupled zones (the bed and the free-board) is considered [15–17] in which the two zones are separated by an interface allowing mass and energy exchanges [2,6,17–20]. Two general types of models are incorporated that are associated with the homogeneous and heterogeneous phases of the process [5,18,21]. Based on the solid phase combustion in the heterogeneous models, one may use continuous models (macro-scale models), which treat the solid phase as a porous medium [6,10, 18,22] and discrete element models (DEM) (micro-scale models), which describe particles in a moving grate [18,23,24]. Currently, most studies have focused primarily on the solid phase combustion in fixed beds, but, the simultaneous Modelling of both the solid and the gas phases is still needing more attention [5,6,11,13,22,25–27].

Gollaza *et al.* studied a transient 3D CFD model for the combustion of densified wood [6]. The computational domain was divided into two zones: a fixed bed described as a porous medium and the free-board. They simulated both the gas and the solid temperature profiles at different positions inside the reactor. Their results reproduced many of the key features of the experiments. Mehrabian *et al.* [5] developed a transient 3D CFD model for biomass combustion in similarly coupled zones (fixed bed and free-board). The authors also measured the gas concentrations of CO, CO_2, CH_4, H_2O, H_2 and O_2 and the temperature at various heights in the reactor for both the bed and the freeboard. Moreover, they evaluated the reaction front velocity. Their predicted results were also in a good agreement with experiments. Sun *et al.* [28] carried out a 2D unsteady CFD using municipal solid waste in a fixed bed reactor. They showed that their predictions of the gaseous species emissions CO, CO_2, O_2 and CH_4 and the temperature profiles at different heights as a function of time for different moisture content were also in agreement with experimental data. These above studies underscore the importance of coupled 2-zone models for fixed bed reactors.

The objective of this study is to investigate numerically the combustion of pellets prepared from oleic by-products, and more precisely, Olive Pits (OPi) in a 40 kW counter-current fixed bed reactor. Indeed, Olive solid wastes (Olive Pomace and Olive Pits) when dried and free of residual oil, could be blended with woody biomass and densified as pellets, briquettes or logs in order to be used as fuels for feeding boilers, stoves and furnaces in many countries such as Spain and Italy. This energy policy is justified by the renewable character of the biomass and by its high heating value reaching 19 MJ/kg. Hence, it is highly important by the present study to simulate the combustion of OPi in a fixed bed reactor in order to give guidance later on the reactor design and geometry, the manner of feeding it by the primary and the secondary air, and on the level of gaseous emissions that should be reduced.

The simulations based on a cylindrical reactor are implemented using a transient 2D configuration using the COMSOL Multiphysics software. Consistently with earlier studies, the computational domain was divided into two zones: the bed and the freeboard zones. Due to the strong coupling of the mass and heat transfer between the two zones, equations describing the various sub-models were solved simultaneously to represent moisture evaporation, VOC devolatilization, pyrolysis, gasification, gas phase combustion and residual char combustion.

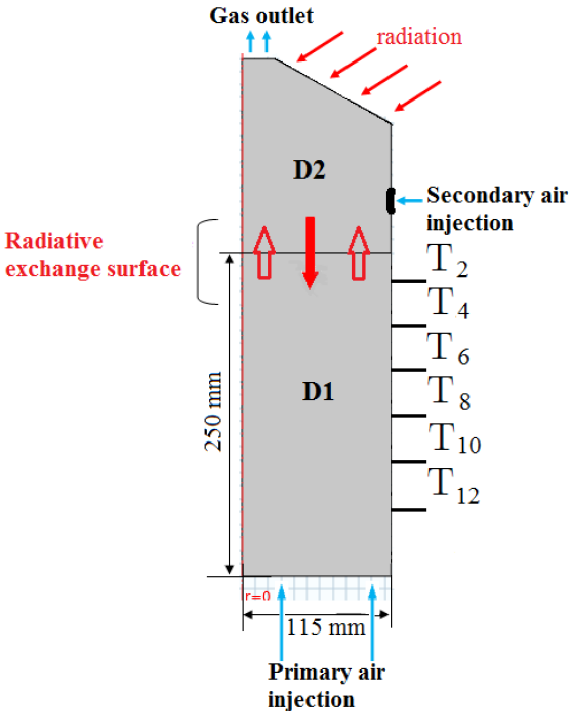

Figure 1. The 2D geometry model.

The homogenous gas phase reactions are modelled for a fuel mixture of CO, CO_2, O_2, CH_4, H_2 and H_2O in the freeboard zone. A weak turbulence $\kappa - \varepsilon$ model is used for turbulence closure. From the simulations, we report the temperature profiles at different heights inside the reactor in the two regions and the gaseous emissions and the mass loss as a function of elapsed time. The CFD were validated using experimental data from a prior experiment [29] as well as additional data reported in the literature [5,11,22,28,30–32].

2. Model description and hypothesis

2.1. *Computational configuration and modelling assumptions*

The 2D axisymmetric model used is a cylindrical geometry with 400 mm height (H) and 115 mm diameter (d) is shown in Figure 1. The cylinder is divided into two zones: the fixed bed denoted (D1) and the freeboard (D2).

The model used to simulate the entire combustion process is based on the following assumptions and conditions:

- The computational domain is divided into two fully coupled zones: the fixed bed and the freeboard.
- The fixed bed is bounded by adiabatic walls and treated as a porous medium.
- In the counter-current configuration, the ignition starts from the top towards the bottom of the bed during which the combustion evolves layer by layer.
- The solid phase and the gas phase are modelled with their own energy equation while allowing for mass and energy exchange between the two zones via a permeable interface.
- The biomass particles are modelled as perfectly spherical and randomly packed.
- The evaporation process occurred at a specific temperature and is assumed thermally controlled.
- The pyrolysis phase of the Olive Pits pellets (OPi) is modelled by a three-step reaction mechanism yielding biogas, tars and Volatile Organic Compounds (VOC).
- The solid fraction and the particles' sizes vary during the residual char combustion and gasification.
- VOC produced during pyrolysis and gasification is mainly CO, CO_2, H_2, CH_4 and H_2O_{vap}. The combustion of the residual char (in the bed zone), CO, H_2 and CH_4 in the freeboard zone governs the entire process.
- The residual char obtained by pyrolysis is gasified by CO_2 and H_2O and oxidized by air. A flame front starts at the top bed and propagates to the bottom with a characteristic speed.
- No assumptions are used concerning the heat transfer and the three modes; conduction, convection and radiation are considered. The radiative transfer is modelled using an effective thermal conductivity.
- The gas emissions and the heat leaving the packed bed (D1) are considered as the inlet conditions for the freeboard zone (D2).
- The bed, which is electrically heated in the experiment, is assumed to be heated by

incident radiative transfer from the walls with a prescribed constant wall temperature, T_{wall}, equals to 1173.15 K.
- The incoming radiation flux from the freeboard region is modelled as an incident radiative heat to the fixed bed.

The reactor is fed by two air inlets: the primary air with a flow rate of 10 Nm^3/h is injected under the bed bottom and passes through the fixed particles. Whereas the secondary air used to enhance the gas phase combustion is introduced at the side of the freeboard zone with a flow rate of 25 Nm^3/h as illustrated in Figure 1. Both air injections occur at an ambient temperature of 298.15 K. In the actual experimental study [29], the fixed bed was equipped with thirteen type K-thermocouples, which are spaced at 20 mm increment along the reactor, but, only six type K-thermocouples (Figure 1) are considered during the present numerical study in order to reduce the simulation time.

2.2. *Modelling of rate processes*

The overall combustion process can be divided into four different sub-processes: drying, pyrolysis and combustion of VOC, and combustion and gasification of the residual char. In this study, the drying process is modelled as a heterogeneous reaction at the solid temperature [32–34]. This process is represented by a first-order kinetic reaction based on the Arrhenius law:

$$\text{Humidity} \xrightarrow{k_v} \text{Water vapor} \tag{1}$$

with

$$k_v = A\exp\left(-\frac{E_v}{RT_s}\right) \tag{2}$$

and

$$\dot{w} = k_v \rho_s Y_{H_2O,s}. \tag{3}$$

Here, A is the frequency factor, E_v is the activation energy and $\dot{w}_{moist}$ is the reaction rate (kg/(m^3·s). The values of these rate constant parameters are given in Table 1.

Pyrolysis is a complex process, which involves a number of coupled chemical reactions [10,35–38]. Here, the lignocellulosic samples containing mainly hemicelluloses, cellulose and lignin produce, via pyrolysis, three products; biogas, tars and biochar. The rate contents of these products depend on the type of samples and especially on the type of pyrolysis (slow, fast or flash). The total devolatilization rate [34] is modelled as follows:

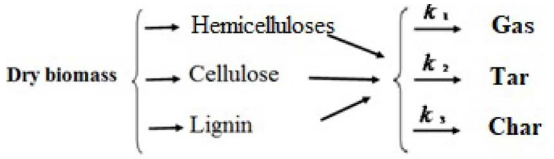

$$\dot{w}_{py} = (K_1 + K_2 + K_3)\rho_{moist} = \rho_{moist}\sum_{i=1}^{3} A_i \exp\left(\frac{E_i}{RT_s}\right) \tag{4}$$

where the rate constant parameters for K_1, K_2 and K_3 are given in Table 1.

The reaction of the combustion and gasification of the residual char is considered as a heterogeneous and exothermic reaction [39,40]. The oxidation of the residual char with the O_2 of injected primary air is described by the following 2-step reactions:

$$C + O_2 \rightarrow CO_2 \tag{5}$$

$$C + \tfrac{1}{2}O_2 \rightarrow CO \tag{6}$$

while the gasification processes with CO_2 and H_2O as gasifier can be represented by:

$$C + H_2O \rightarrow H_2 + CO \tag{7}$$

$$C + CO_2 \rightarrow 2CO \tag{8}$$

The reaction rates of (5)–(8) are estimated using the following expressions:

$$\dot{w}_C^{O_2} = K_1 [O_2]; \quad K_1 = A_1 \exp\left(-\frac{E_1}{RT_s}\right) \tag{9}$$

$$\dot{w}_C^{O_2} = K_2 [O_2]^{0.5}; \quad K_2 = A_2 \exp\left(-\frac{E_2}{RT_s}\right) \tag{10}$$

$$\dot{w}_C^{H_2O} = K_3 [H_2O]; \quad K_3 = A_3 \exp\left(-\frac{E_3}{RT_s}\right) \tag{11}$$

$$\dot{w}_C^{CO_2} = K_4 [CO_2]; \quad K_4 = A_4 \exp\left(-\frac{E_4}{RT_s}\right). \tag{12}$$

The combustion of gaseous emissions is modelled using the following reactions:

$$CH_4 + \tfrac{1}{2}O_2 \rightarrow 2H_2 + CO,$$

$$\text{with } \dot{w}_{CH_4} = A_5 [CH_4] [O_2]^{0.5} \exp\left(\frac{E_5}{RT_g}\right) \tag{13}$$

$$CO + O_2 \rightarrow CO_2,$$

$$\text{with } \dot{w}_{CO} = A_6 [O_2] [CO] \exp\left(\frac{E_6}{RT_g}\right) \tag{14}$$

$$H_2 + O_2 \rightarrow H_2O,$$

$$\text{with } \dot{w}_{H_2} = A_7 [O_2] [H_2] \exp\left(\frac{E_7}{RT_g}\right). \tag{15}$$

The values of the different constants A_i and E_i are given in Table 1. The parameters presented in Table 1 are not taken from literature because there isn't any

Table 1. Rate constant's parameters

Olive pits pellets	Pre-exponential factor A (1/s)	Activation energy E (kJ/mol)
Drying	1.06×10^3	88.5
Pyrolysis		
Cellulose	2×10^{12}	185
Hemicellulose	3.5×10^{11}	105
Lignin	10^8	192
Tar	1.5×10^5	192
Residual char combustion	9×10^8	2.25×10^5 (k_1)
	7×10^9	1.3×10^3 (k_2)
Residual char gasification	1.6×10^6	2.2×10^4 (k_3)
	3.5×10^7	225×10^4 (k_4)
Combustion of pyrolysis gases	10^7	1.89×10^5 (k_5)
	1.674×10^5	1.25×10^3 (k_6)
	1.95×10^7	1.67×10^5 (k_7)

reported work using the same fuel type as us. Hence, we are inspired by a similar reported work in the literature [11] to calibrate our model so that it matches our previous experimental results [29].

2.3. *Governing equations in the fixed bed and the freeboard*

Solid and gas phase equations are solved as a transient two-dimensional formulation in cylindrical coordinates. Various conservation equations describing the fuel conversion of mass, momentum and energy were solved in two coupled zones as reported in literature for similar studies [2–4,10–13]. The gases emitted from the bed, CO, CO_2, H_2 and CH_4, and their composition are prescribed as inlet conditions for the freeboard zone. These gases are likely to react with oxygen in the secondary air. In order to lighten the text to the readers, all equations with meanings of all variables and parameters are provided in Appendices A and B.

2.4. *Fuel properties*

The size of the olive solid by-products pellets as olive pits used in our numerical simulation ranged from approximately 2.5 to 3.5 cm and with an equivalent diameter up to 6 mm. Ultimate analysis as %C, %H, and %O and proximate analysis as Volatile Matter (%VM), %Ash and Fixed Carbone (%C) and energy contents as the bulk density of the olive solid by-products pellets are assumed to be the same as the values published in [29]. On the other hand, the ash content evolution is not taken into account.

2.5. *Mesh and numerical resolution*

The finite element method was used to discretize the unsteady governing equations. To establish grid convergence, we considered 5 mesh resolutions, which are summarized in Table 3.

Calculations show that the meshes named coarse or normal did not yield grid convergence. However, finer or extra-fine meshes required extensive computational times four to five weeks on a mini-workstation. The "fine" mesh resolution provides a reasonable compromise where grid convergence is established while a reasonable computational time of approximately 24 h is achieved. The corresponding mesh size is approximately 1.5 mm, whereas the calculation time was automatically defined by the solver.

Finally, a moving mesh was adopted in order to refine our calculations at the interface between the two computational zones as shown on Figure 2.

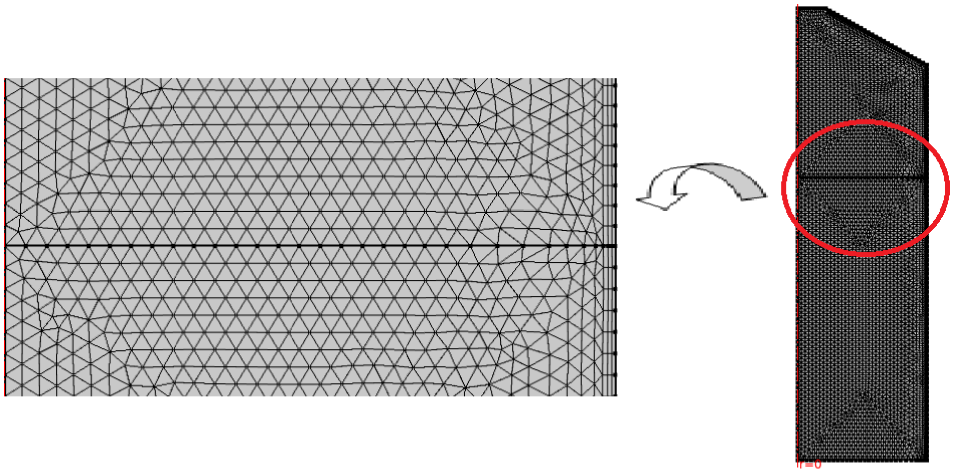

Figure 2. Mesh grid structure.

Table 2. Summary parameter's values and correlations

Property	Correlation/value	Reference
Permeability	$K_R = \dfrac{d_p^2 \varepsilon_s^2}{180(1-\varepsilon_s^2)}$	[41]
Solid thermal conductivity	$\lambda_s = \varepsilon_s \lambda_g + \sum_i Y_i \lambda_i$ $\lambda_{\text{rad}} = 4\varepsilon_s \sigma \omega d_p T_s^3$	[10,42,43]
Emissivity	0.9	
Bed porosity	0.5	
Specific surface	$S_p = \dfrac{6(1-\varepsilon_s)}{d_p}$	
Heat transfer coefficient	$h_{sg} = \dfrac{N_u \lambda_{\text{eff},g}}{d_p} = -h_{gs}$	
Nusselt number	$N_u = 2 + 1.1 R_e^{0.6} P_r^{1/3}$	
Gas density	$\rho_g = \dfrac{pM_g}{RT_g}$	

3. Results and discussion

3.1. *Mass loss*

The accurate prediction of the temporal evolution of the mass loss of the olive pit pellets is an important test of the overall performance of the computational study. This mass loss is prescribed by the following equation:

$$\frac{\partial m}{\partial t} = -\sum_{i=1}^{4} \dot{w}_i. \tag{16}$$

Accounts for the contributions of all relevant reaction processes that include: drying, pyrolysis, combustion and gasification of the residual char [5,44]. In (16), the $\dot{w}_i$ represents the reaction rates associated with each process (kg/m^3·s).

Figure 3 compares the temporal evolutions of the modelled (dashed) and measured (solid) mass loss [29]. The comparison shows a good agreement between measurements and computations. The mass loss could be divided into three phases (I), (II) and (III) on Figure 3: the first phase (I) corresponds to moisture evaporation, the second phase (II) corresponds to the devolatilization and combustion of gases, and. the final phase (III) corresponds to the residual char combustion. Similar

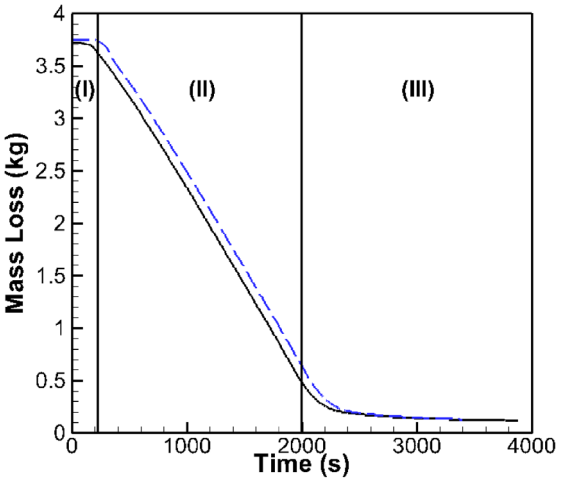

Figure 3. Mass loss history. Experiment (solid), Simulation (dashed).

Table 3. Different mesh resolutions considered with their boundary and domain elements

Meshes	Domain elements	Boundary elements
Coarse	2,129	154
Normal	4,525	224
Fine	7,305	285
Finer	11,176	354
Extra-fine	49,944	748

results were reported in literature for both numerical simulations [14,45] and experimental measurements [46–48].

3.2. *Temperature and gas velocity evolutions inside the reactor*

The temporal evolution of the temperature distribution inside the reactor is shown in Figure 4. The figure also serves to highlight the propagation of the combustion processes both in the freeboard zone and in the fixed bed. As shown, ignition started from the top at $t = 0$ s, and then the flame propagates rapidly in the gas phase. This process continues into the solid phase, yet at a slower rate, until the bottom of the bed is reached [31].

However, the gas velocity profile as a function of the radial distance of the reactor, as illustrated in Figure 5, reveals that the gas flows in the opposite direction to the ignition front propagation, hence, the counter-current nature of the bed [49]. The decrease of the temperature near the interface between the gas and solid phases can be attributed to convective cooling associated with secondary air [26,50]. For a height up to approximately 0.3 m, the gas velocity profile remains flat ($\approx$0.075 m·s^{-1}). However, as the mixture of gases and secondary air reach the activation temperature, the combustion in the gas phase is started and the gas velocity increases rapidly reaching about 5 m/s. This is a typical value for gas phase combustion [26].

To better understand the combustion process in the fixed bed, we attempt to look closely at the solid phase combustion. Figure 6 compares the computed and measured temperature profiles of the olive pit pellets at different heights along the reactor centreline corresponding to 5, 45, 85 and 165 mm, which also correspond to 4 different placements of the thermocouples in the experiment [29,51]. The simulation was undertaken under the same experimental conditions with a primary air flowrate of 10 Nm^3/h injected at ambient conditions (10^5 Pa, 298.15 K). The secondary air flowrate was 25 Nm^3/h under the same standard conditions of temperature and pressure. The figure shows a reasonable agreement between computation and experiment, exhibiting both similar temporal trends and magnitudes.

The discrepancy between experimental and simulated temperature (overestimation of its maximum) can be attributed to two possible sources. First, radiative absorption is not taken into account in our computations. Species like CO_2, CO and water vapour are characterized by reasonably high absorption coefficients. Second, the presence of ash subject to melting and agglomeration at high temperatures may inhibit the air circulation through the porous medium. Nevertheless, these results show again that the self-sustained progression of the combustion front evolves from the upper to the lower layers of the bed. In addition, the appearance of an odd little peak at a given time for every fixed bed depth corresponds to the condition of maximum efficiency of reactivity because of maximum yields of CO, H_2 and C_{org} as it is shown on Figure 8. Consequently, there is a maximum heat release by reactions manifesting with a maximum temperature.

Figure 7 compares computed temporal evolutions of temperature of the solid and gas phases inside the fixed bed (zone D1) at the 5 different thermo-

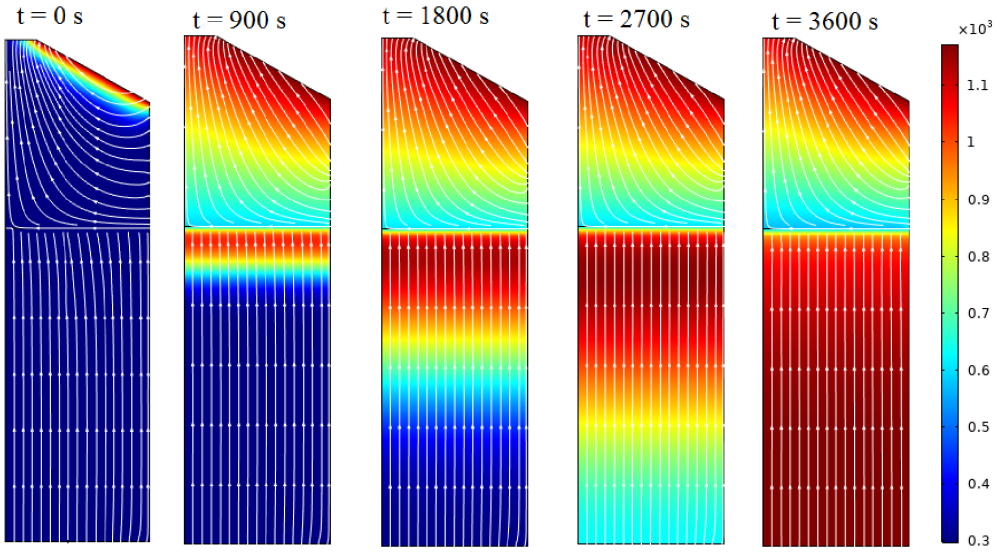

Figure 4. The temperature distribution inside the reactor at different instants.

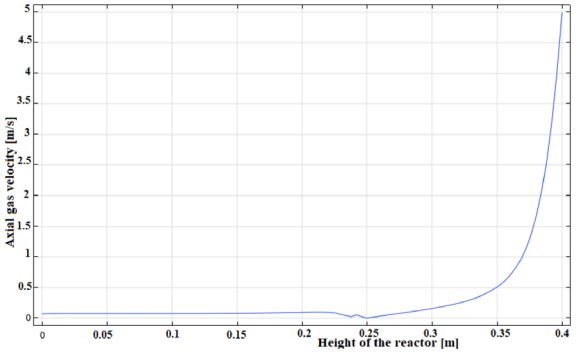

Figure 5. Gas velocity profile.

couple positions corresponding to 2, 45, 85, 165 and 205 mm. The result shows that both solid and gases phases are in thermal equilibrium inside the porous medium. Hence, it is possible to consider a single energy conservation equation and to exclude the convective term between the gas phase and the solid phase. Such an assumption can greatly simplify the model formulation and improve the efficiency of the computations.

3.3. *Gaseous emissions in the freeboard zone*

Figure 8 compares the temporal evolutions of the computed and measured gaseous emissions for O_2, CO, CO_2, H_2, CH_4, H_2O_g, and C_{org} whenever such comparisons are available. We observe the presence of discrepancies between simulated and experimental profiles: There is temporal delay between curves and simulated profiles do not exhibit the fluctuations observed in the experimental results. We believe that the discrepancy may be attributed to ash accumulation, which prevents the inlet air circulation. Moreover, the physical presence of thermocouples could affect measurements, but above all, the kinetics of reactivity should be improved.

The increase of water vapour concentration can be attributed to the fuel evaporation and to the combustion of H_2 and CH_4 as shown in (15) and (18). Moreover, the sudden decrease of O_2 concentration marks the onset of the combustion process. This process is accompanied by an increase in CO_2 and CO concentrations. One observes that the concentration of CO_2 increases rapidly and remains at a roughly constant level of about 15% (against around 14% for the experiment measurements). In contrast, the increase of concentration of CO and H_2 could be explained by the gasification of the residual char in the presence of gasifiers CO_2 and water vapour, not to mention the contributions of CH_4 reactions described by (9), (10) and (15). Moreover, the behaviour of methane gas is similar to what was reported in some numerical simulation studies in literature [4,44,52]. A decrease in H_2O, H_2, CO and CO_2 was noted at the end of the combustion process

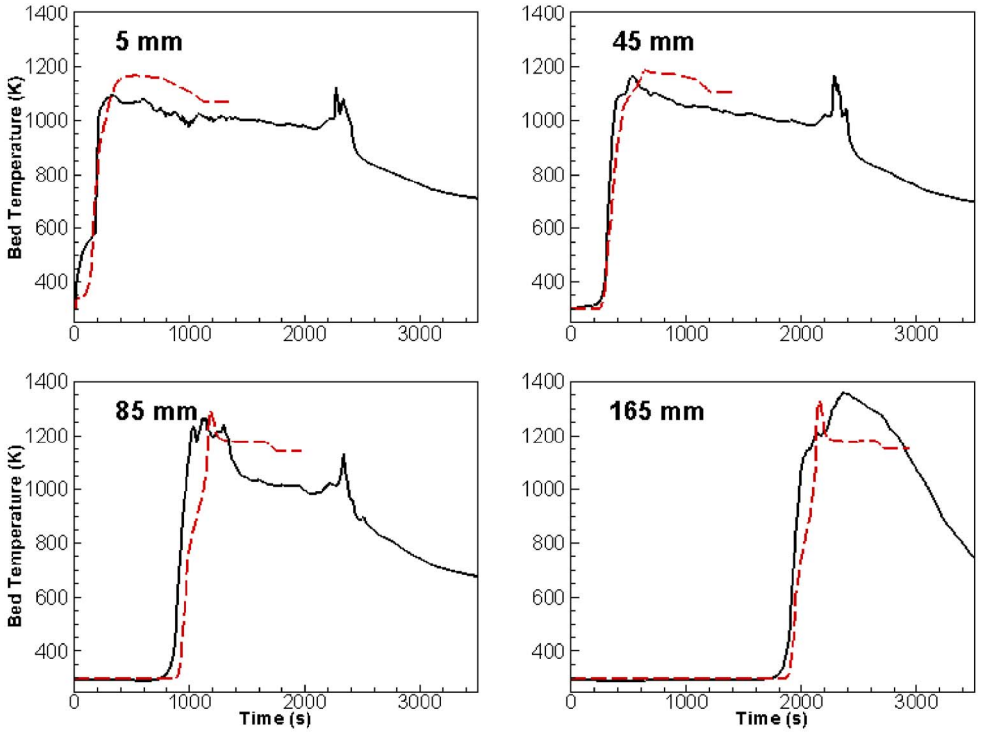

Figure 6. Comparison of temperature profiles obtained numerically and experimentally. Experiment (solid), Simulation (dashed).

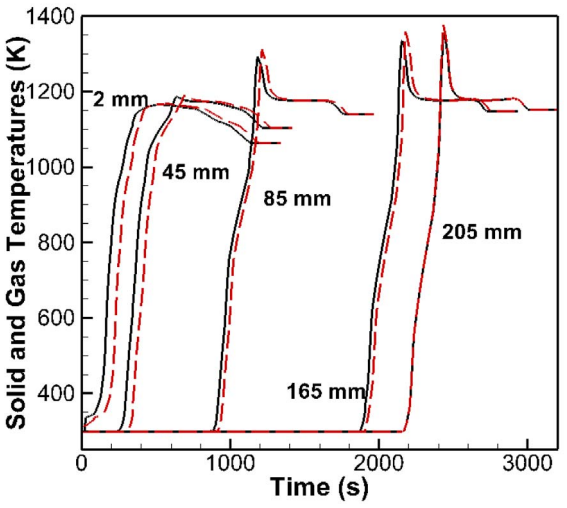

Figure 7. Simulated temperatures of the solid and gas inside the fixed bed (D1 zone). Solid temperature (solid), gas temperature (dashed).

(the fuel is completely consumed), while the O_2 mole fraction is again 21%.

Regardless, the slight difference between the simulation and the experiment in Figure 8 can be due to the sub models associated with the flow, turbulence and chemistry as well as the choice of the axisymmetric geometry. Also, during the experiment measurements certain systematic and non-systematic errors may be at the source of some fluctuations.

4. Characteristic parameters

Some characteristic parameters, which describe the combustion behaviour including the reaction front velocity, the mass conversion rate and the ignition rate are obtained from the measurements can be modelled. The comparisons of the temporal evolution of these parameters are shown in Figures 9a and b as a function of time. The comparison between these measurements and calculated parameters shows a relatively good agreement. However, these dependencies characteristics can provide a basis to transfer the fixed bed reactor to the situation of a grate incinerator.

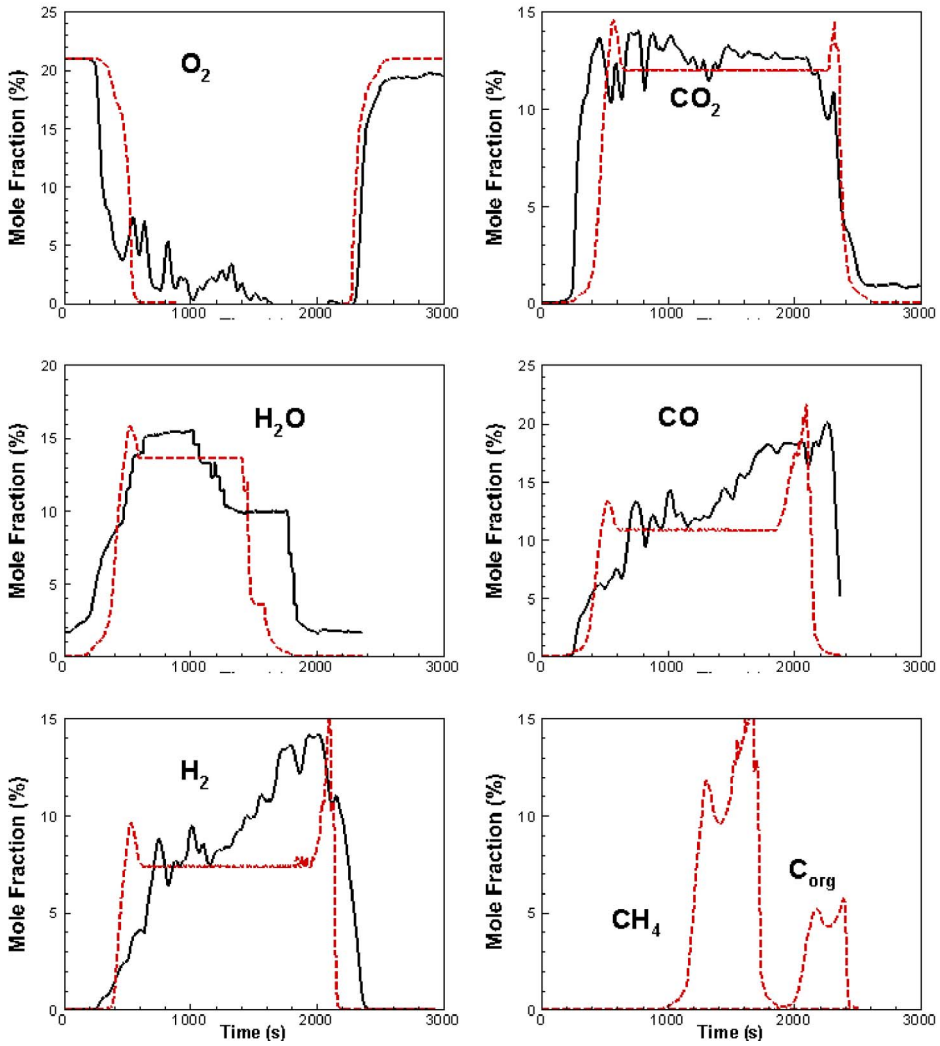

Figure 8. Gaseous emissions in the freeboard zone: comparison between simulated and experimental results. Experiment: Solid, Simulation: Dashed.

5. Main variables evolution in the model

Finally, we present profiles of the mass densities of the solid fraction (top left), the char density (top right), the moisture density (bottom left) and the dry olive pits pellets density (bottom right). These computed profiles are compared to those of the experiment in Figure 10. These modelled results correspond to the CFD simulations for the fixed bed reactor (zone D1) at time $t = 3900$ s and a primary airflow equal to 310 kg·h^{-1}·m^{-2}. The figure shows that a large zone of char density remains constant at the vicinity of 170 kg·m^{-3}. In this large zone, the primary airflow injection may not have been sufficient for a rapid consumption of the generated char. Consequently, this may have delayed the homogenous reaction of the char. This observation was also reported in the literature for the same conditions of airflow (0.05 kg·s^{-1}·m^{-2}) [49].

6. Conclusion

A transient 2D axisymmetric CFD simulation was carried out to simulate the multiphase combustion

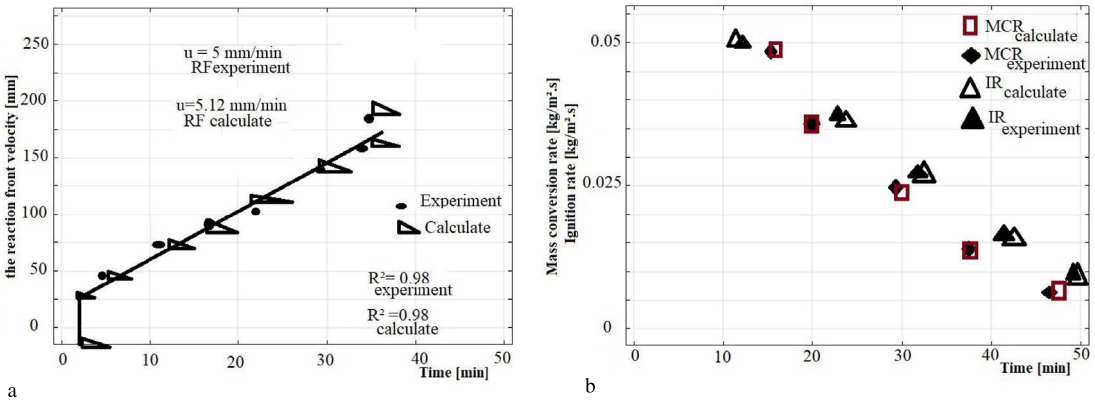

Figure 9. (a) A comparison between the measurement and the calculated of the reaction front velocity. (b) A comparison between the measurement and the calculated of the mass conversion rate and the ignition rate.

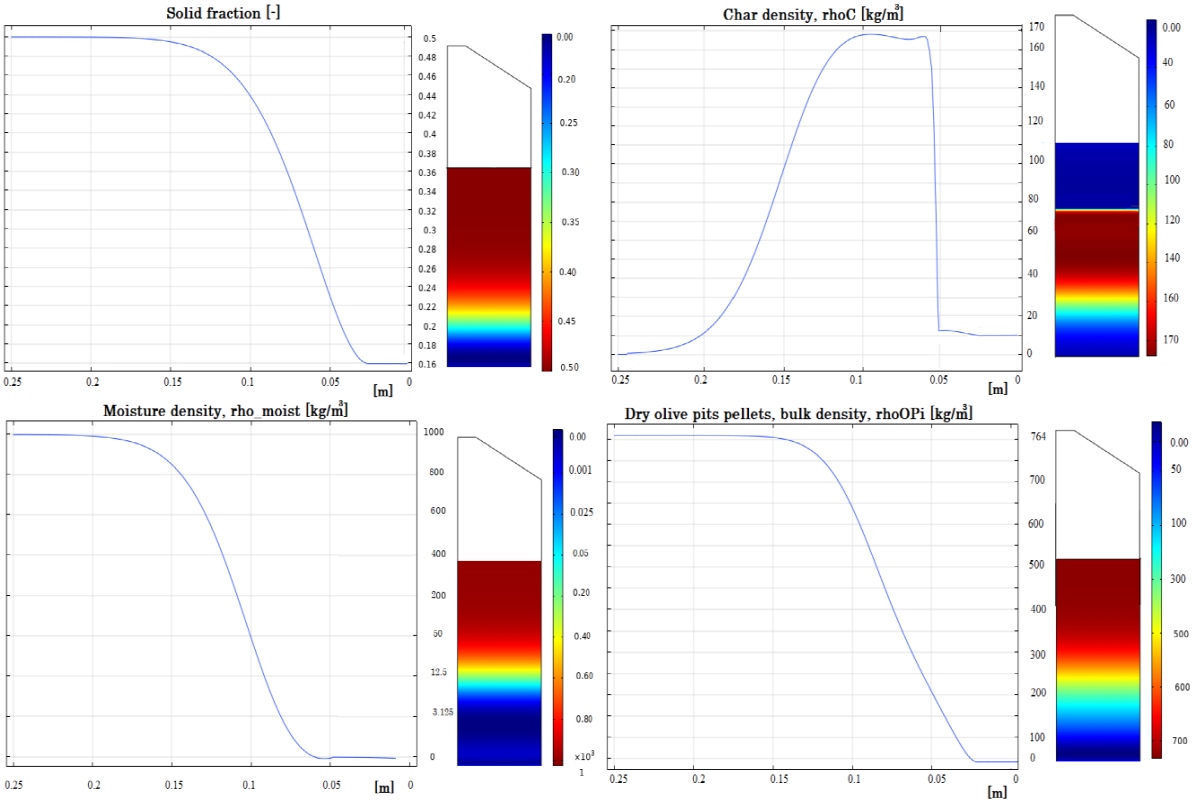

Figure 10. Evaluation of solid fraction and densities of char, moisture, and dry olive pits pellets at 3900 s.

of lignocellulosic solid biofuels (olive pits pellets) in a counter-current fixed bed reactor. The simulations were implemented using COMSOL Multiphysics 5.5. The reactor is divided into two zones: D1 and D2 representing the fixed bed and the freeboard. Reduced kinetic schemes were used in the solid and the gas

phases. Moreover, an Euler/Euler approach was used to model the porous fixed bed. The turbulent flow was described by the $k-\varepsilon$ model. Results show that the present formulation adequately reproduces experimental observations related to over-the-bed gas concentrations, temperatures and mass loss. Calculated characteristic parameters like reaction front velocity, mass conversion rate and ignition rate are reproduced in close agreement with the experiment. However, the models developed for the pilot scale fixed bed reactor can be extended to an industrial-scale plant for example using an incinerator grate.

Nomenclature

u	Velocity	$\mathrm{m{\cdot}s^{-1}}$
A	Pre-exponential factor	$\mathrm{s^{-1}}$
D	Diffusion coefficient	$\mathrm{m^2{\cdot}s^{-1}}$
Y	Mass fraction	–
S_i	Source term	$\mathrm{kg{\cdot}m^{-3}{\cdot}s^{-1}}$
p	Pressure	Pa
g	Gravitational acceleration constant	$\mathrm{m{\cdot}s^{-2}}$
C_p	Specific heat	$\mathrm{J{\cdot}kg^{-1}{\cdot}K^{-1}}$
S	Surface	$\mathrm{m^{-2}}$
h	Convective heat transfer coefficient	$\mathrm{W{\cdot}m^{-2}{\cdot}K^{-1}}$
ΔH_R	Enthalpy of reaction	$\mathrm{J{\cdot}kg^{-1}}$
Q_{rad}	Radiative source	$\mathrm{W{\cdot}m^{-3}}$
d	Diameter	m
E	Activation energy	$\mathrm{J{\cdot}kmol^{-1}}$
S_k	Source term of the turbulent energy production	$\mathrm{kg{\cdot}m^{-1}{\cdot}s^{-3}}$
S_ϵ	Source term of turbulent dissipated energy	$\mathrm{kg{\cdot}m^{-1}{\cdot}s^{-4}}$
T	Temperature	K
X, x	Mole fraction	–
R	Ideal gas constant	$\mathrm{J{\cdot}mol^{-1}{\cdot}K^{-1}}$
$\dot{w}$	Reaction rate	$\mathrm{kg{\cdot}m^{-3}{\cdot}s^{-1}}$
t	Time	s
H	Reactor height	m
z	Axial position	m
r	Net production rate of the gas species	$\mathrm{kg{\cdot}m^{-3}{\cdot}s^{-1}}$
M	Atomic molar mass	$\mathrm{kg{\cdot}mol^{-1}}$
N_u	Nusselt number	–
R_e	Reynolds Number	–
P_r	Prandtl Number	–
k	Turbulent kinetic energy	$\mathrm{m^2{\cdot}s^{-2}}$
K_R	Permeability	$\mathrm{m^2}$
r	Radial position	m
$\dot{m}$	Air flow	$\mathrm{kg{\cdot}s^{-1}}$
a	Bed cross-section	$\mathrm{m^2}$
k_i	Kinetic rate constant	$\mathrm{s^{-1}}$
f	Pressure loss	$\mathrm{N{\cdot}m^{-3}}$

Greek symbols

ε	Porosity	–
λ	Thermal conductivity	$\mathrm{W{\cdot}m^{-1}{\cdot}K^{-1}}$
μ	Dynamic viscosity	Pa·s
ρ	Density	$\mathrm{kg{\cdot}m^{-3}}$
σ	Stefan–Boltzmann constant	$\mathrm{W{\cdot}m^{-2}{\cdot}K^{-4}}$
ϵ	Turbulent kinetic energy dissipation	$\mathrm{m^2{\cdot}s^{-3}}$
λ	Stoichiometric air coefficient	–
β	Absorption coefficient	–
ω	Emissivity	–
α	Mass of the compound i produced per kg of pyrolyzed	–
$\sigma_{i,j}$	collision cross-section	Å
$\Omega_{i,j}$	collision integral	–
$\tau_{i,j}$	Stress tensor	–

Subscripts

app	Apparent
eff	Effective
t	Total
rad	Radiation
pyr	Pyrolysis
g	Gas
s	Solid
i, j	Relating to components I and j
p	Particle
v	Vaporisation
a	Ash
c or C	Carbon
CFD	Computational Fluid Dynamics

Conflicts of interest

Authors have no conflict of interest to declare.

Appendix A. Solid phase modelling

The mass conservation for the moisture, the dry OPi pellets and the residual char, respectively, are written as:

$$\frac{\partial(\varepsilon_s\rho_m)}{\partial t} = \dot{w}_{\text{moist}}\varepsilon_s \tag{17}$$

and

$$\frac{\partial(\varepsilon_s\rho_{\text{dry,olive}})}{\partial t} = -\dot{w}_{\text{pyr}}\varepsilon_s \tag{18}$$

$$\frac{\partial\left(\varepsilon_s\rho_{\text{C}}\right)}{\partial t} = (\dot{w}_{\text{pyr}} - \dot{w}_{\text{C}}^{\text{H}_2\text{O}} - \dot{w}_{\text{C}}^{\text{CO}_2} - \dot{w}_{\text{C}}^{\text{O}_2})\varepsilon_S. \tag{19}$$

The solid fraction conservation is as follows:

$$\frac{\partial\varepsilon_s}{\partial t} = \left(\frac{-\dot{w}_{\text{C}}^{\text{H}_2\text{O}} - \dot{w}_{\text{C}}^{\text{CO}_2} - \dot{w}_{\text{C}}^{\text{O}_2}}{\rho_s}\right)\varepsilon_s. \tag{20}$$

In order to take into account the bed shrinkage, the following expression is considered:

$$\frac{\partial d_p^3}{\partial t} = \left(\frac{-\dot{w}_{\text{C}}^{\text{H}_2\text{O}} - \dot{w}_{\text{C}}^{\text{CO}_2} - \dot{w}_{\text{C}}^{\text{O}_2}}{\rho_s}\right)d_p^3 \tag{21}$$

while the ash component is assumed to be inert:

$$\frac{\partial\left(\varepsilon_s\rho_a\right)}{\partial t} = 0. \tag{22}$$

In the above conservation equations; $\dot{w}_{\text{moist}}$, $\dot{w}_{\text{pyr}}$, $\dot{w}_{\text{C}}^{\text{H}_2\text{O}}$, $\dot{w}_{\text{C}}^{\text{CO}_2}$ and $\dot{w}_{\text{C}}^{\text{O}_2}$ are the rates of evaporation, pyrolysis, gasification, and combustion of the char, respectively. Accordingly, the total density can be calculated as:

$$\rho_s = Y_{\text{moist}}\rho_{\text{moist}} + Y_{\text{olive}}\rho_{\text{olive}} + Y_{\text{C}}\rho_{\text{C}}. \tag{23}$$

The energy equation is expressed as:

$$\frac{\partial\left(\varepsilon_s C_{p,s}\rho_s T_s\right)}{\partial t} - \frac{\partial}{\partial z}\left(\lambda_{\text{eff},s}\frac{\partial T_s}{\partial z}\right) - \frac{1}{r}\frac{\partial}{\partial r}\left(r\lambda_{\text{eff},s}\frac{\partial T_s}{\partial r}\right) = A_p h_{sg}\left(T_g - T_s\right) + S_s + Q_{\text{rad}}. \tag{24}$$

Here $\lambda_{\text{eff},s}$ is the solid thermal effective conductivity calculated as the sum of the solid phase conductivity and radiation, A_p is the specific surface area, h_{sg} is the convective heat transfer coefficient given in Table 2. S_s and Q_{rad} are two source terms that represent the heat release rate and radiation source, respectively. The latter is modelled as [10,15]:

$$Q_{\text{rad}}(z) = \beta\sigma(\omega_{\text{rad}}T_{\text{wall}}^4 - \omega_s T_s^4) \tag{25}$$

where, β is the absorption coefficient related to the particle diameter and the solid fraction:

$$\beta = -\frac{1}{d_p}\ln(\varepsilon_s). \tag{26}$$

The specific heat of the solid phase C_{ps} is evaluated in terms of the specific heats of its components using:

$$C_{p,s} = Y_{\text{H}_2\text{O}}C_{p,\text{H}_2\text{O}} + Y_C C_{p,C} + Y_{\text{ash}}C_{p,\text{ash}} + Y_{\text{char}}C_{p,\text{char}}. \tag{27}$$

The enthalpy is calculated as:

$$\begin{aligned}\text{H}_s = {} & \dot{w}_{\text{dry}}L_v(T_s) - \dot{w}_{\text{C}}^{\text{O}_2}\Delta_r h_{\text{C}}(T_s) \\ & - \dot{w}_{\text{C}}^{\text{H}_2\text{O}}\Delta_r h_{\text{C}}(T_s) - \dot{w}_{\text{C}}^{\text{CO}_2}\Delta_r h_{\text{C}}(T_s) \\ & - \dot{w}_{\text{dry}}(1-\alpha_{\text{C}})\Delta_r h_{\text{pyr}}(T_s)\end{aligned} \tag{28}$$

and the species conservation is insured by:

$$\frac{\partial}{\partial t}\left(\varepsilon\rho_s Y_{i,s}\right) = S_{i,s}. \tag{29}$$

Here the index i represents, the moisture, the char, and the ash, respectively.

Appendix B. The gas phase governing equations

The continuity equation and the energy conservation in the gas phase are expressed as follows:

$$\frac{\partial\left(\varepsilon_g\rho_g\right)}{\partial t} + \frac{1}{r}\frac{\partial\left(r\rho_g u_{g,r}\right)}{\partial r} + \frac{\partial\left(\rho_g u_{g,z}\right)}{\partial z} = \dot{w}_{\text{moist}} + \dot{w}_{\text{pyr}} + \dot{w}_{\text{char}} \tag{30}$$

$$\begin{aligned}&\frac{\partial}{\partial t}\left(\varepsilon_g C_{p,g}\rho_g T_g\right) + \frac{1}{r}\frac{\partial}{\partial r}\left(r\rho_g C_{p,g}u_{g,z}T_g\right) \\ &\quad + \frac{\partial}{\partial z}(\rho_g C_{p,g}u_{g,z}T_g) + \frac{1}{r}\frac{\partial}{\partial r}\left(r\rho_g\lambda_{\text{eff},g}\frac{\partial T_g}{\partial r}\right) \\ &= \frac{1}{r}\frac{\partial}{\partial r}\left(r\lambda_{\text{eff},g}\frac{\partial T_g}{\partial r}\right) + \frac{\partial}{\partial z}\left(\lambda_{\text{eff},g}\frac{\partial T_g}{\partial z}\right) \\ &\quad + \text{A}_p\text{h}_{\text{gs}}\left(T_{\text{S}} - T_g\right) - \sum_i \dot{w}_i\Delta H_i + \Phi\end{aligned} \tag{31}$$

where

$$\Phi = \sum_i r_{\text{prod},i}\int_{T_g}^{T_s} c_{\text{prod},i}\,\text{d}T. \tag{32}$$

Here, the index i represents the modelled species in the gas phase, CO_2, CH_4, H_2, CO, O_2 and H_2O_g. $\lambda_{\text{eff},g}$ is the gas thermal conductivity and $r_{\text{prod},i}$ is the rate of reaction of gaseous species. $u_{g,r}$ and $u_{g,z}$ are the radial and azimuthal gas velocity components, respectively.

Note that the thermal conductivity, the specific heat and the dynamic viscosity of the gas phase are all temperature and composition dependent. The specific heat is expressed as the weighted sum of the

species' specific heats weighted by their mass fractions of all constituents:

$$c_{p,g}(T) = \sum_i Y_i c_{p,i}(T_g) \tag{33}$$

where Y_i is the ith species mass fraction.

The thermal conductivity and the dynamic viscosity of the gas phase are expressed by [53]:

$$\lambda_g = \sum_i \left(\frac{x_i \lambda_{i,g}}{\sum_j x_i \varphi_{i,j}} \right) \tag{34}$$

$$\mu_g(T_g) = \sum_i \left(\frac{x_i \mu_i(T_g)}{\sum_j x_i \phi_{i,j}} \right). \tag{35}$$

$\varphi_{i,j}$ and ϕ_{ij} were taken directly from the literature [54]. Also, the effective thermal conductivity of the gas inside the reactor is calculated by the following correlation [34]:

$$\lambda_{\text{eff},g} = 0.8\lambda_g + 0.5 d_p c_{p,g} \rho_g \frac{u_g}{\varepsilon}. \tag{36}$$

The momentum equations in the radial and azimuthal directions are expressed by:

$$\begin{aligned}
&\frac{\partial}{\partial t}\left(\varepsilon_g \rho_g u_{g,r}\right) + u_r \frac{\partial}{\partial r}\left(\rho_g u_{g,r}\right) + u_z \frac{\partial}{\partial z}\left(\rho_g u_{g,r}\right) \\
&\quad = -\frac{\partial p}{\partial r} + \mu_e \left(\frac{1}{r}\frac{\partial}{\partial z}\left(r \frac{\partial u_{g,r}}{\partial z} \right) + \frac{1}{r}\frac{\partial}{\partial r}\left(r \frac{\partial u_{g,z}}{\partial r} \right) \right. \\
&\qquad \left. + \frac{\partial^{2u_{g,r}}}{\partial z^2} - 2\frac{u_{g,r}}{r^2} \right) + \mu_e \frac{\partial}{\partial z}\left(\frac{\partial u_{g,r}}{\partial r} \right) \\
&\qquad - \frac{2}{3}\frac{\partial}{\partial r}\left(\mu_e \left(\frac{1}{r}\frac{\partial}{\partial r}\left(r u_{g,r} \right) + \frac{\partial u_{g,z}}{\partial z} \right) + \rho k \right) \\
&\qquad + \varepsilon_g \rho_g g_r + f_r
\end{aligned} \tag{37}$$

with,

$$f_r = \frac{180 \mu_g u_{g,r} (1-\varepsilon_s)}{d^2 p \varepsilon_s^2} + \frac{1.75 \rho_g u_{g,r}^2}{d^2 p \varepsilon_s^2} \tag{38}$$

and

$$\begin{aligned}
&\frac{\partial}{\partial t}\left(\varepsilon_g \rho_g u_z\right) + u_{zr} \frac{\partial}{\partial r}\left(\rho_g u_z\right) + u_z \frac{\partial}{\partial z}\left(\rho_g u_z\right) \\
&\quad = -\frac{\partial p}{\partial z} + \mu_e \left(\frac{1}{r}\frac{\partial}{\partial r}\left(r \frac{\partial u_z}{\partial r} \right) + \frac{1}{r}\frac{\partial}{\partial r}\left(r \frac{\partial u_r}{\partial z} \right) + \frac{\partial^{2u_z}}{\partial z^2} \right) \\
&\qquad - \frac{2}{3}\frac{\partial}{\partial}\left(\frac{1}{r}\frac{\partial}{\partial r}\left(r u_r \right) + \frac{\partial u_z}{\partial z} + \rho k \right) + \varepsilon_g \rho_g g_z + f_r.
\end{aligned} \tag{39}$$

Here, the effective viscosity, μ_e, is expressed as the sum of the molecular dynamic viscosity and the turbulence viscosity.

$$\mu_e = \mu_g + \mu_t. \tag{40}$$

The turbulent viscosity μ_t, is expressed in terms of the turbulence kinetic energy, k, and its dissipation, ϵ, as follows.

$$\mu_t = \rho C_\mu \frac{k^2}{\epsilon} \quad \text{where } C_\mu = 0.09. \tag{41}$$

Here, k and ϵ are modelled using a standard low-Reynolds number $k-\epsilon$ model [55]. The species conservation equations are given by:

$$\begin{aligned}
&\frac{\partial}{\partial t}\left(\varepsilon \rho_g X_{i,g}\right) + \frac{1}{r}\frac{\partial}{\partial r}\left(r \rho_g u_{g,z} X_{i,g} \right) + \frac{\partial}{\partial z}\left(\rho_g u_{g,z} X_{i,g} \right) \\
&\quad = \frac{1}{r}\frac{\partial}{\partial r}\left(r D_{\text{eff},g} \rho_g \frac{\partial X_{i,g}}{\partial r} \right) + \frac{\partial}{\partial z}\left(D_{\text{eff},g} \rho_g \frac{\partial X_{i,g}}{\partial z} \right) + S_i.
\end{aligned} \tag{42}$$

The dispersion coefficient of the gaseous species $D_{\text{eff},g}$ is obtained according to the following correlation [10,56], which accounts for the contribution of mass diffusion and the presence of a packed bed:

$$D_{\text{eff},g} = 0.8 D_{gi,j} + 0.5 \mu_g \frac{d_p}{\varepsilon}. \tag{43}$$

In which $D_{gi,j}$ is the ith species molecular diffusivity. This mixture-averaged diffusion is evaluated using the binary diffusion coefficient, which is modelled using the Chapman–Enskog correlation [56]:

$$D_{gi,j} = 8.380 \frac{\sqrt{\frac{1}{M_i} + \frac{1}{M_i}}}{\sigma_{i,j}^2 \Omega_{i,j}} \left(\frac{T_g}{T_0} \right)^{1.81} \tag{44}$$

where T_0 is a reference temperature. The last term in the right-hand side of (42), S_i, corresponds to the ith species reaction rate.

References

[1] A. Agrifoglio, A. Fichera, A. Gagliano, R. Volpe, *C. R. Chim.*, 2021, **24**, 39-55.

[2] M. A. Gómez, J. Porteiro, D. De la Cuesta, D. Patiño, J. L. Míguez, *Energy Convers. Manage.*, 2017, **140**, 260-272.

[3] C. Yin, L. Rosendahl, S. K. Kær, S. Clausen, S. L. Hvid, T. Hille, *Energy Fuels*, 2008, **22**, 1380-1390.

[4] Y. Menard, "Modélisation de l'incinération sur grille d'ordures ménagères et approche thermodynamique du comportement des métaux lourds", PhD Thesis, Institut National polytechnique de Lorraine-INPL, 2003, Sciences de l'Ingénieur [physics].

[5] R. Mehrabian, A. Shiehnejadhesar, R. Scharler, I. Obernberger, *Fuel*, 2014, **122**, 164-178.

[6] J. Collazo, J. Porteiro, D. Patiño, E. Granada, *Fuel*, 2012, **93**, 149-159.

[7] A. Shiehnejadhesar, R. Scharler, R. Mehrabian, I. Obernberger, *Fuel Process. Technol.*, 2015, **139**, 142-158.

[8] A. Shiehnejadhesar, R. Mehrabian, R. Scharler, G. M. Goldin, I. Obernberger, *Fuel*, 2014, **126**, 177-187.

[9] M. Buchmayr, J. Gruber, M. Hargassner, C. Hochenauer, *Energy Convers. Manage.*, 2016, **115**, 32-42.
[10] N. T. M. Duffy, J. A. Eaton, *Combust. Flame*, 2013, **160**, 2204-2220.
[11] H. Mätzing, H.-J. Gehrmann, H. Seifert, D. Stapf, *Waste Manage.*, 2018, **78**, 686-697.
[12] C. Bruch, B. Peters, T. Nussbaumer, *Fuel*, 2003, **82**, 729-738.
[13] M. A. Gómez, J. Porteiro, D. De la Cuesta, D. Patiño, J. L. Míguez, *Fuel*, 2016, **184**, 987-999.
[14] B. Khiari, F. Marias, F. Zagrouba, J. Vaxelaire, *J. Clean. Prod.*, 2008, **16**, 178-191.
[15] A. Zhou, H. Xu, W. Yang, Y. Tu, M. Xu, W. Yu *et al.*, *Energy Fuels*, 2018, **32**, 9493-9505.
[16] Z. Yu, X. Ma, Y. Liao, *Renew. Energy*, 2010, **35**, 895-903.
[17] C. Galletti, V. Giomo, S. Giorgetti, P. Leoni, L. Tognotti, *Appl. Therm. Eng.*, 2016, **96**, 372-384.
[18] A. Dernbecher, A. Dieguez-Alonso, A. Ortwein, F. Tabet, *Biomass Convers. Biorefin.*, 2019, **9**, 129-182.
[19] Y. Wang, L. Yan, *Int. J. Mol. Sci.*, 2008, **9**, 1108-1130.
[20] B. Rajh, C. Yin, N. Samec, M. Hriberšek, M. Zadravec, *Energy Convers. Manage.*, 2016, **125**, 230-241.
[21] D. Merrick, *Fuel*, 1983, **62**, 534-539.
[22] Y. B. Yang, Y. R. Goh, R. Zakaria, V. Nasserzadeh, J. Swithenbank, *Waste Manage.*, 2002, **22**, 369-380.
[23] A. Anca-Couce, N. Zobel, H. A. Jakobsen, *Fuel*, 2013, **103**, 773-782.
[24] A. H. Mahmoudi, X. Besseron, F. Hoffmann, M. Markovic, B. Peters, *Chem. Eng. Sci.*, 2016, **142**, 32-41.
[25] I. Haberle, Ø. Skreiberg, J. Łazar, N. E. L. Haugen, *Prog. Energy Combust. Sci.*, 2017, **63**, 204-252.
[26] J. K. A. T. Rajika, M. Narayana, *SpringerPlus*, 2016, **5**, article no. 1166.
[27] A. Galgano, C. Di Blasi, A. Horvat, Y. Sinai, *Energy Fuels*, 2006, **20**, 2223-2232.
[28] R. Sun, T. M. Ismail, X. Ren, M. Abd El-Salam, *Waste Manage.*, 2015, **39**, 166-178.
[29] M. A. Mami, H. Mätzing, H.-J. Gehrmann, D. Stapf, R. Bolduan, M. Lajili, *Energies*, 2018, **11**, article no. 1965.
[30] R. Buczyński, R. Weber, A. Szlek, R. Nosek, *Energy Fuels*, 2012, **26**, 4767-4774.
[31] M. A. Gómez, J. Porteiro, D. Patiño, J. L. Míguez, *Fuel*, 2014, **117**, 716-732.
[32] M. Markovic, E. A. Bramer, G. Brem, *Waste Manage.*, 2014, **34**, 49-62.
[33] M. Sreekanth, D. R. Sudhakar, B. V. S. S. S. Prasad, A. K. Kolar, B. Leckner, *Fuel*, 2008, **87**, 2698-2712.
[34] H. Khodaei, Y. M. Al-Abdeli, F. Guzzomi, G. H. Yeoh, *Energy*, 2015, **88**, 946-972.
[35] Y. B. Yang, R. Newman, V. Sharifi, J. Swithenbank, J. Ariss, *Fuel*, 2007, **86**, 129-142.
[36] B. Miljković, I. Pešenjanski, M. Vićević, *Fuel*, 2013, **104**, 351-364.
[37] M. Boutaleb, M. Guiza, S. Román, B. L. Cano, S. Nogales, A. Ouederni, *C. R. Chim.*, 2020, **23**, 607-621.
[38] N. Boukaous, L. Abdelouahed, M. Chikhi, C. Mohabeer, A. H. Meniai, B. Taouk, *C. R. Chim.*, 2020, **23**, 623-634.
[39] A. A. Azzaz, M. Jeguirim, E. A. N. Marks, C. Rad, S. Jellali, M.-L. Goddard, C. M. Ghimbeu, *C. R. Chim.*, 2020, **23**, 635-652.
[40] S. Kordoghli, B. Khiari, M. Paraschiv, F. Zagrouba, M. Tazerout, *Int. J. Hydrog. Energy*, 2019, **44**, 11289-11302.
[41] P. Xu, B. Yu, *Adv. Water Resour.*, 2008, **31**, 74-81.
[42] P. Kaushal, J. Abedi, N. Mahinpey, *Fuel*, 2010, **89**, 3650-3661.
[43] R. Johansson, H. Thunman, B. Leckner, *Combust. Flame*, 2007, **149**, 49-62.
[44] J. Li, M. C. Paul, P. L. Younger, I. Watson, M. Hossain, S. Welch, *Appl. Energy*, 2015, **156**, 749-755.
[45] A. K. Biswas, K. Umeki, *Chem. Eng. J.*, 2015, **274**, 181-191.
[46] A. K. Biswas, M. Rudolfsson, M. Broström, K. Umeki, *Appl. Energy*, 2014, **119**, 79-84.
[47] C. Ryu, Y. B. Yang, A. Khor, N. E. Yates, V. N. Sharifi, J. Swithenbank, *Fuel*, 2006, **85**, 1039-1046.
[48] S. Varunkumar, N. K. S. Rajan, H. S. Mukunda, *Combust. Sci. Technol.*, 2011, **183**, 1147-1163.
[49] H. Thunman, B. Leckner, *Fuel*, 2003, **82**, 275-283.
[50] J. Porterio, D. Patiño, J. L. Miguez, E. Granada, J. Moran, J. Collazo, *Combust. Flame*, 2012, **159**, 1296-1302.
[51] M. A. Mami, M. Lajili, B. Khiari, M. Jeguirim, *Fuel*, 2020, **277**, article no. 118181.
[52] M. A. Gómez, J. Porteiro, D. Patiño, J. L. Míguez, *Fuel*, 2014, **117**, 716-732.
[53] R. B. Bird, W. E. Stewart, E. N. Lightfoot, *Transport Phenomena Revised*, 2nd ed., John Wiley & Sons, New York, 2007.
[54] J. Gosse, *Techniques de l'ingénieur Caractérisation et propriétés de la matière*, 1991.
[55] J.-C. Lezcano-Benítez, D. Correa-Restrepo, A.-A. Amell-Arrieta, F.-J. Cadavid-Sierra, *CT&F - Cienc. Tecnol. Futuro*, 2011, **4**, 89-104.
[56] W. J. Massman, *Atmos. Environ.*, 1998, **32**, 1111-1127.